

Impact of lower limb movement on the hemodynamics of femoropopliteal arteries: A computational study

*Original*

Impact of lower limb movement on the hemodynamics of femoropopliteal arteries: A computational study / Colombo, M.; Luraghi, G.; Cestariolo, L.; Ravasi, M.; Airoidi, A.; Chiastra, C.; Pennati, G.. - In: MEDICAL ENGINEERING & PHYSICS. - ISSN 1350-4533. - 81:(2020), pp. 105-117. [10.1016/j.medengphy.2020.05.004]

*Availability:*

This version is available at: 11583/2859519 since: 2021-01-04T17:00:19Z

*Publisher:*

Elsevier

*Published*

DOI:10.1016/j.medengphy.2020.05.004

*Terms of use:*

This article is made available under terms and conditions as specified in the corresponding bibliographic description in the repository

*Publisher copyright*

(Article begins on next page)

# Impact of lower limb movement on the hemodynamics of femoropopliteal arteries: a computational study

Monika Colombo<sup>1\*</sup>, Giulia Luraghi<sup>1\*</sup>, Ludovica Cestariolo<sup>1</sup>, Maddalena Ravasi<sup>1</sup>, Anna Airoidi<sup>1</sup>,  
Claudio Chiastra<sup>1,2</sup>, Giancarlo Pennati<sup>1</sup>

\*equally contributed

1. Laboratory of Biological Structure Mechanics (LaBS), Department of Chemistry, Materials and Chemical Engineering “Giulio Natta”, Politecnico di Milano, Milan, Italy
2. PoliTo<sup>BIO</sup>Med Lab, Department of Mechanical and Aerospace Engineering, Politecnico di Torino, Turin, Italy

## Corresponding author:

Dr. Claudio Chiastra, PhD

PoliTo<sup>BIO</sup>Med Lab

Department of Mechanical and Aerospace Engineering

Politecnico di Torino

Corso Duca degli Abruzzi, 24

10129 Turin, Italy

E-mail: [claudio.chiastra@polito.it](mailto:claudio.chiastra@polito.it)

ORCID: <http://orcid.org/0000-0003-2070-6142>

## Abstract:

Femoropopliteal arteries (FPAs) are subjected to a wide range of deformations, mainly determined by leg movement. FPAs are often affected by atherosclerotic plaque development, presumably influenced by the biomechanics of surrounding tissues. Although abnormal hemodynamics in FPAs appears to be an important factor in driving plaque development, to date it has been investigated in few studies, in which the leg was modeled in either fixed straight or bent configuration. Hence, the current work investigates the impact of leg movement on FPA hemodynamics.

An idealized model of FPA was created to perform moving-boundary computational fluid dynamics analyses. By mimicking hip rotation, knee flexion and complete movement of walking, the hemodynamics was compared between moving- and fixed-boundary models. Moreover, additional features affecting the hemodynamics (e.g. flow-rate curve amplitude, walking speed) were examined.

Relevant hemodynamic differences were found between the moving- and fixed-boundary models, with the leg movement inducing higher time-averaged wall shear stress (TAWSS) (up to 66%). The flow-rate amplitude and walking period were the most influential parameters (differences in TAWSS up to 68% and 74%, respectively).

In conclusion, this numerical approach highlighted the importance of considering leg movement to investigate FPA hemodynamics, and it could be employed in future patient-specific analyses.

**Keywords:** femoropoplital artery, moving leg, computational fluid dynamics, moving boundary, wall shear stress

### Abbreviations

FPA	femoropopliteal artery
WSS	wall shear stress
CFD	computational fluid dynamics
SFA	superficial femoral artery
PA	popliteal artery
TA	tibial artery
HRP	hip reference point
KRP	knee reference point
ARP	ankle reference point
TAWSS	time-averaged wall shear stress
OSI	oscillatory shear index
RRT	relative residence time

## 1. Introduction

The femoropopliteal artery (FPA), which crosses the hip and the knee joint structures, is the longest artery of the human body. This vascular segment is frequently narrowed by atherosclerotic plaques, the leading cause of the occlusive peripheral artery disease [1], which affects more than 8 million individuals in the United States only and has an expected increasing incidence [2]. Moreover, once treated, the FPA is characterized by a high rate of restenosis, which can exceed the 30% in case of stenting procedures [3].

Besides common vascular risk factors for both atherosclerosis and restenosis, such as diabetes mellitus and cigarette smoking [1], it has been hypothesized that FPA is widely subjected to these pathologies because of its anatomy and its peculiarly complex biomechanics [4]. In fact, due to the pulsatility of arterial blood flow and the leg movement [5,6], the FPA undergoes multiple, cyclic deformation modes. Among them, radial and longitudinal compression, bending and torsion, induce a complex state of solicitation within the vessel wall and likely affect the local hemodynamics.

Abnormal hemodynamics, characterized by low and oscillatory wall shear stress (WSS), has been recognized as a major biomechanical factor promoting atherosclerotic plaque development [7–9] and neointima hyperplasia [10]. However, at the present the majority of studies have focused on coronary and carotid arteries rather than FPA. Only in the last 15 years, the interest for the FPA hemodynamics has emerged, with an increasing number of computational studies [11–18]. Different models of straight and bent FPA were developed to investigate the impact of relevant structural effects, such as kinking and pinching, on hemodynamics [17,18]. However, none of the previous works examined the impact of dynamic, cyclic leg movement.

According to the types of leg movement, which are expected to create different hemodynamic effects, FPA can be divided into two distinct regions: (i) the vascular segment running behind the knee, which undergoes cyclic geometrical and pronounced curvature changes in case of knee flexion [19], and (ii) the straight-like vascular segments upstream and downstream the knee, which are mainly

rigidly moving and then subjected to mere inertial effects. Despite it was hypothesized that frequent leg movement and, consequently, frequent changes of arterial shape might redistribute the lumen regions exposed to low WSS, with a possible delay of the atherosclerotic process [20], the hemodynamic characterization of a moving FPA during its movement is still lacking.

Accordingly, the aim of this work is to investigate the impact of the leg movement on the local hemodynamics of FPA by means of computational fluid dynamics (CFD) simulations. Specifically, an idealized numerical model of healthy FPA is created by considering its typical dimensions and curvature changes. The use of an idealized geometry is preferred to enhance the effects merely related to the leg movement, without introducing additional contributions due to other features such as vessel tortuosity, local wall irregularities or bifurcations.

In order to assess the relative role of inertial effects and cyclic curvature changes of the different FPA portions, three leg movements are simulated: (i) hip rotation with a rigidly extended leg, (ii) knee flexion with fixed thigh and (iii) complex movement as during walking, with a combination of hip rotation and knee flexion based on gait analysis data. CFD simulations are then performed comparing moving- with fixed-boundary straight and bent FPA models. Furthermore, since the leg movement is not related to the heartbeat, the impact of a phase difference between cardiac and bending cycles, their amplitude and period are analyzed on the moving-boundary FPA model of walking.

## 2. Methods

### 2.1. Idealized CFD model of the femoropopliteal artery

An idealized model of the FPA was built as a cylinder with a diameter of 5.5 mm [21] and a length of 400 mm [22]. The vessel geometry was divided into three parts (Figure 1-A): (i) the proximal portion running parallel to the femur, corresponding to a segment of the superficial femoral artery (SFA); (ii) the central portion, representing the popliteal artery (PA); and (iii) the distal portion running parallel to the tibia, corresponding to the proximal tibial artery (TA). The diameter of the vessel geometry was kept constant along the entire length of the model and was representative of the PA, which is the vessel region most affected by knee bending. Moreover, three reference points external to the vessel were added to the model to represent the articular joints of the hip (HRP), the knee (KRP), and the ankle (ARP).

The FPA model was discretized into tetrahedral elements with five prism layers at the wall, characterized by a growth scale factor of 1.1. A mesh independence study was conducted in a moving-boundary FPA model ( $M_{\text{walking}}$ , for details see next section) by progressively doubling the mesh element number. The mean velocity in the whole fluid domain and WSS were chosen as monitor variables. The solution was assumed as independent from the mesh when the differences between the solutions of two consecutive mesh refinements were less than 1%. After this analysis, a mesh with 1,061,941 elements (mean element size of 0.55 mm) was selected (Figure 1-B). The discretization phase was performed using ANSA Pre Processor v19.0 (BETA CAE Systems, Switzerland).

Blood was modeled as an incompressible and Newtonian fluid, with a density of  $1060 \text{ kg/m}^3$  and dynamic viscosity of 3.5 cP. A flat velocity profile, based on a typical femoral artery triphasic waveform [16] with period of 1 s and mean inlet flow-rate of 120 mL/min [23] (Figure 1-C), was imposed as inflow boundary condition, while zero-pressure and no-slip conditions were applied at the outlet and at the wall, respectively. The flow was assumed as laminar since the maximum Reynolds number at peak flow-rate was 250.

Both moving- and fixed- boundary CFD simulations were performed on the idealized model of the FPA. All the simulations were performed using the incompressible fluid solver (ICFD) implemented in the finite element software LS-DYNA 971 R11 (LSTC, Livermore, CA, USA). Residuals for pressure and momentum equations were set to  $10^{-6}$ . A constant time step size of  $5 \cdot 10^{-4}$  s was chosen based on the Courant-Friedrichs-Lewy condition. An analysis of the repeatability of the results over the cardiac cycles was also carried out by monitoring the mean velocity and WSS in the moving-boundary FPA model adopted in the mesh independence study. The variables were evaluated at four significant time instants of the cardiac cycle, *i.e.* peak of flow-rate, mid-inversion phase, reflux peak and mid-constant phase. Results differed less than 1.5% between the first two cycles. Consequently, two cardiac cycles were considered as sufficient to guarantee a repeatable solution. All investigated cases are detailed in the following two sections.

## 2.2. Moving-boundary CFD analysis

To analyse the effect of both anatomy and dynamic movement on local hemodynamics of FPA, flexions of the vessel at the level of the hip and knee joints were modeled by means of moving-boundary CFD simulations. Specifically, the leg movement was imposed to the vessel wall (structure domain) to move the fluid domain, with an Arbitrary Lagrangian-Eulerian kinematic algorithm [24].

Under movement imposition, the SFA and TA portions were forced to rotate rigidly, parallel to the femur and the tibia, respectively. This simplifying assumption was justified by the fact that those parts are anatomically embedded in the muscles. Instead, the bent configuration of the PA, not constrained by the muscles at the level of the hiatus channel, was drawn by connecting the SFA and TA portions with three circumference arcs (Figure 2-A). These arcs were defined to provide the vessel a shape mimicking the in-vivo shape and to guarantee the observed shortening of the PA during the knee flexion (showing a non-linear behavior with the knee flexion angle - Figure 2-B) [4,6,25,26].

Three types of leg movement were reproduced: (i) hip rotation with the leg rigidly extended (model  $M_{\text{hip}}$ ), (ii) knee flexion with fixed thigh (model  $M_{\text{knee}}$ ) and (iii) complete movement of walking

(model  $M_{\text{walking}}$ ). The hip rotation and knee flexion movements went from a straight configuration to a  $90^\circ$  rotation of the hip or the knee, respectively. For those two movements, seven configurations were drawn, interpolated, and imposed to the vessel wall with a sinusoidal pattern with a period of 1 s, as schematically shown in Figures 2-C and 2-D. For the complete movement of walking, from the coordinates in time of HRP, KRP and ARP (see Figure 1-A), nine reconstructed configurations were used to impose two walking cycles with a single period ( $T_{\text{bending}}$ ) of 1 s (Figure 2-E). For each movement under investigation, the simplification of a planar vessel displacement was assumed.

### 2.3. Impact of leg movement and sensitivity analysis

Fixed-boundary simulations were carried out on straight (model  $F_0$ ),  $13^\circ$ -bent (model  $F_{13}$ ),  $45^\circ$ -bent (model  $F_{45}$ ),  $58^\circ$ -bent (model  $F_{58}$ ), and  $90^\circ$ -bent leg configurations (model  $F_{90}$ ), and compared with the corresponding configurations of the moving-boundary models, used as reference. Furthermore, to investigate the impact of several parameters (i.e. phase difference between the bending and inlet flow-rate cycles, the flow-rate curve amplitude and the walking speed) on FPA hemodynamics, simulations changing one parameter at a time were performed and compared to the reference model  $M_{\text{walking}}$ . In particular, the influence of the phase difference between the bending and the inlet flow-rate cycles was analysed by starting the bending movement halfway through the cardiac cycle (model  $M_{\text{phase}}$ ). The influence of the flow-rate amplitude and of the walking speed was assessed by doubling and halving the flow-rate (models  $M_{2Q}$  and  $M_{Q/2}$ ) and the  $T_{\text{bending}}$  (models  $M_{2T}$  and  $M_{T/2}$ ), respectively. Figure 3 presents an overview of the models, the analyses and the performed comparisons.

### 2.4. Analysis of the results

The results of the moving- and fixed- boundary CFD simulations were analyzed in terms of velocity field at specific time instants of the cardiac cycle ( $T_1$ - $T_6$ , Figure 1-C) and WSS-based descriptors. In particular, three common cardiac cycle-averaged WSS-based descriptors, namely the

time-averaged wall shear stress (TAWSS), the oscillatory shear index (OSI) and the relative residence time (RRT), were quantified for each model, as indicated:

$$TAWSS = \frac{1}{T} \int_0^T |\mathbf{WSS}| dt \quad (1)$$

$$OSI = 0.5 \left[ 1 - \left( \frac{|\int_0^T \mathbf{WSS} dt|}{\int_0^T |\mathbf{WSS}| dt} \right) \right] \quad (2)$$

$$RRT = \frac{1}{(1-2 \cdot OSI) \cdot TAWSS} \quad (3)$$

where  $T$  is the cardiac period. Furthermore, as conducted in previous studies [27,28], the WSS-based descriptors computed at each node of all cases were combined to define objective thresholds: the 33<sup>th</sup> percentile was identified for TAWSS, the 66<sup>th</sup> percentile for OSI and RRT. The following thresholds were found: 0.62 Pa, 0.23 and 2.59 Pa<sup>-1</sup> for TAWSS, OSI and RRT, respectively. Then, the percentage of luminal area exposed to TAWSS (OSI and RRT) lower (or higher) than the so-defined thresholds was computed and named TAWSS33 (OSI66 and RRT66).

### 3. Results

#### 3.1. Impact of the leg movement type

To evaluate the impact of the leg movement type applied on the FPA model, the instantaneous velocity field of the models  $M_{hip}$ ,  $M_{knee}$  and  $M_{walking}$  was analyzed at different time instants (Figures 4, 5 and 6, respectively). Moreover, the WSS-based descriptors were computed for  $M_{hip}$ ,  $M_{knee}$  and  $M_{walking}$  and reported in Table 1, 2 and 3, respectively, considering the whole FPA model (i.e. Total) and the three vessel portions of interest (i.e. SFA, PA and TA).

##### 3.1.1. Hip rotation: $M_{hip}$

At the time instants  $T_1$  and  $T_4$ , when the leg movement was negligible, the velocity patterns were uniform within the whole FPA model (Figure 4-A and C). Whereas, at  $T_3$  and  $T_5$ , when the angular

velocity of the leg was maximum, the velocity patterns were not uniform along the vessel axis, with the velocity magnitude was maximum in the TA (~2.5 m/s) and minimum in the SFA (~1 m/s) (Figure 4-B and D). The impact of the inertial effect due to limb movement was relevant, as highlighted by the different velocity field in the whole FPA model at  $T_4$  and  $T_5$ , which are time instants characterized by similar diastolic flow-rate but different angular velocity of the leg.

As regards the WSS-based descriptors (Table 1), while the mean OSI was identical in all the portions of the model (0.35), the mean TAWSS and RRT were maximum in the SFA (1.95 Pa and  $2.27 \text{ Pa}^{-1}$ , respectively) and minimum in the PA (1.80 Pa and  $2.00 \text{ Pa}^{-1}$ , respectively).

### 3.1.2. Knee flexion: $M_{knee}$

At  $T_1$  and  $T_4$ , when the angular velocity of the leg was negligible, the velocity patterns were dependent only on the straight or bent vessel configuration. Specifically, at  $T_1$  the velocity patterns were similar along the vessel axis (Figure 5-A). Conversely, at  $T_4$  the velocity profile was symmetric in the SFA and skewed towards the outer wall in the distal portions PA and TA (Figure 5-C). As found for the model  $M_{hip}$ , at  $T_3$  and  $T_5$ , when the angular velocity of the leg was maximum, the impact of the inertial effect due to limb movement was relevant, resulting in non-uniform velocity patterns along the vessel axis (Figure 5-B and D). At both time instants, the velocity magnitude was maximum in the TA (~0.8 m/s) and minimum in the SFA (~0 m/s).

Regarding the WSS-based descriptors (Table 2), the mean TAWSS increased going from the SFA to the TA portion (from 0.64 to 0.88 Pa). The maximum mean OSI was found in the TA (0.17), while a lower OSI value (0.13) characterized the SFA and PA portions. The mean RRT decreased moving from the SFA to the TA (from  $2.63$  to  $1.88 \text{ Pa}^{-1}$ ).

### 3.1.3. Walking: $M_{walking}$

Figure 6-A shows that the velocity magnitude on the longitudinal section of the FPA model markedly changed during the walking cycle. At  $T_1$ ,  $T_2$  and  $T_6$ , the velocity patterns were not uniform

along the vessel axis, with maximum velocity magnitude in the TA, which was characterized by the highest inertial effects due to limb movement, and minimum in the SFA (Figure 6B-D).

Concerning the WSS-based descriptors (Table 3), the maximum mean TAWSS was found in the SFA and TA (0.93 Pa). The PA was characterized by a lower value (0.84 Pa). Similarly, higher values of mean OSI and RRT were present in the SFA and TA as compared to the central portion of the model.

#### **3.1.4. Comparison among $M_{hip}$ , $M_{knee}$ and $M_{walking}$**

As previously pointed out, the leg movement type influenced the velocity field in all moving-boundary FPA models (Figures 4-6). In all cases, the highest influence of the inertial effects due to limb movement on the velocity patterns was observed in the PA and TA portions of the model and increased moving away from the HRP. As reported in Tables 1-3,  $M_{hip}$  was characterized by higher values of mean TAWSS and OSI in the whole vessel as compared to the others while  $M_{walking}$  presented the highest value of mean RRT. Both  $M_{hip}$  and  $M_{walking}$  showed a negligible lumen area exposed to TAWSS33 (i.e. low TAWSS).  $M_{hip}$  presented the highest area exposed to OSI66 (i.e. high OSI) while  $M_{walking}$  of RRT66 (i.e. high RRT).

### **3.2. Moving- vs. fixed-boundary models**

The moving-boundary CFD analyses were compared to the fixed-boundary ones at specific configurations assumed by each moving-boundary FPA model during the cardiac cycle. The results of the comparison between  $M_{hip}$  and  $F_0$ , between  $M_{knee}$  and  $F_0$ ,  $F_{45}$  and  $F_{90}$ , and between  $M_{walking}$  and  $F_0$ ,  $F_{13}$  and  $F_{58}$  are detailed below.

#### **3.2.1. $M_{hip}$ vs. $F_0$**

As it emerges from Tables 1 and 1-Suppl, the differences in terms of mean TAWSS and OSI between  $M_{hip}$  and  $F_0$  were high in the whole FPA model (>66 % and >53 %, respectively) and similar

in each vessel portion of interest. The differences in terms of mean RRT were lower but still not negligible (>13 %). Overall, the leg movement changed the location of the lumen areas exposed to low WSS, high OSI and RRT (Figure 7-A). Quantitatively, while in  $M_{hip}$  the percentage of lumen area exposed to TAWSS33 was 0 %, in the corresponding fixed-boundary model it was 24 % (Table 1). The opposite was observed for high OSI and RRT with  $M_{hip}$  and  $F_0$  characterized by 99 % and 0 % of lumen area exposed to OSI66, and 29 % and 1 % of lumen area exposed to RRT66 (Table 1).

### 3.2.2. $M_{knee}$ vs. $F_0$ , $F_{45}$ and $F_{90}$

The difference between  $M_{knee}$  and the corresponding fixed-boundary models (i.e.  $F_0$ ,  $F_{45}$  and  $F_{90}$ ) in terms of mean TAWSS in the whole FPA model was ~10 % (Tables 2 and 2-Suppl). The largest differences were found in the distal portion of the vessel (TA, 26 - 29 %) while the smallest ones in the proximal portion (SFA, 3 - 6 %). Also the differences in terms of mean OSI and RRT in the whole FPA model were around 10 % (Tables 2 and 2-Suppl). The largest differences in terms of mean OSI were found in the PA for  $F_0$  (28 %) and in the TA for  $F_{45}$  (10 %) and  $F_{90}$  (26 %). Regarding the mean RRT (Tables 2 and 2-Suppl), while the largest differences were present in the TA for all fixed-boundary models (>14 %), the lowest ones were in the SFA and were ~0 % for models  $F_0$  and  $F_{45}$ .

By comparing the lumen areas exposed to low TAWSS and high OSI and RRT (Figure 7-B), it emerged that the location of those areas was similar in the models  $M_{knee}$  and  $F_{45}$  except for the areas with low TAWSS, which were extended to the PA and TA in case of the fixed-boundary model. Accordingly, different percentages of lumen areas exposed to TAWSS33 were found comparing  $M_{knee}$  against  $F_0$ ,  $F_{45}$  and  $F_{90}$ . (Table 2). Moreover, considering only the fixed-boundary models, a greater angle of knee flexion was associated with larger areas exposed to TAWSS33 (from 24 % in  $F_0$  to 48 % in  $F_{90}$ ). Comparable and low values of lumen area exposed to OSI66 were found in  $M_{knee}$  (1 %) and in the fixed-boundary models (0 % for  $F_0$  and  $F_{45}$ , 1 % for  $F_{90}$ ) (Table 2). Similar lumen areas exposed to RRT66 were found in all cases (~10 %), except for the straight fixed-boundary model (1 %) (Table 2).

### 3.2.3. $M_{walking}$ vs. $F_0$ , $F_{13}$ and $F_{58}$

$M_{walking}$  represents the most complete case, including a combination of both hip rotation and knee flexion. This moving-boundary model was compared against the corresponding fixed-boundary ones  $F_0$ ,  $F_{13}$  and  $F_{58}$  by analysing both the velocity field and the WSS-based descriptors.

As shown by Figure 6, the leg movement had a relevant impact on the velocity field. Both at the systole and diastole, the velocity patterns of  $M_{walking}$  were different as compared to those of  $F_0$ ,  $F_{13}$  and  $F_{58}$  (Figure 6 B-D). In particular, in  $M_{walking}$  the velocity was maximum in the TA and minimum in the SFA. Conversely, in the fixed-boundary models, the velocity patterns were more uniform along the whole FPA model.

High differences were found between  $M_{walking}$  and the corresponding fixed-boundary models in terms of mean TAWSS (~30 %) and OSI (> 36 %) in the whole FPA model (Tables 3 and 3-Suppl). Although not negligible, smaller differences (from 2 to 13 %) were present in terms of mean RRT (Tables 3 and 3-Suppl). In all cases, the central portion of the vessel (i.e. PA) had smaller differences of mean WSS-based descriptors as compared to the proximal and distal portions (i.e. SFA and TA, respectively). As depicted in Figure 7-C, the location of the lumen areas exposed to low TAWSS and high OSI and RRT was different between the moving- and fixed-boundary models (results shown only for  $M_{walking}$  and  $F_{58}$ ). Quantitatively, while in  $M_{walking}$  the percentage of lumen area exposed to TAWSS<sub>33</sub> was 1% in the fixed-boundary models ranged from 24% ( $F_0$ ) to 94 % ( $F_{13}$ ) (Table 3). On the contrary, while in  $M_{walking}$  the percentage of lumen area exposed to OSI<sub>66</sub> was 54 %, in the fixed-boundary models was 0 % (Table 3). Finally,  $M_{walking}$  presented a greater percentage area exposed to RRT<sub>66</sub> (36 %) as compared to the moving-boundary models, with  $F_0$  characterized by the lowest value (1 %) (Table 3).

### 3.3. Moving-boundary simulations: sensitivity analysis

The introduction of a phase difference between the bending and inlet flow-rate cycles in  $M_{\text{phase}}$  resulted in a difference of 21 %, 13 % and 17 % in terms of mean TAWSS, OSI and RRT in the whole FPA model with respect to the reference  $M_{\text{walking}}$  (Tables 4 and 4-Suppl). The percentage of lumen areas exposed to low TAWSS and high OSI and RRT was different between the two models (Table 4) and differently located along the vessel (Figure 8). The greatest difference was related to the low TAWSS, with  $M_{\text{walking}}$  and  $M_{\text{phase}}$  characterized by 1 % and 44 % of lumen areas exposed to TAWSS<sub>33</sub>, respectively.

The change of the flow-rate amplitude or the walking speed had a greater impact on the WSS-descriptors than the phase shift (Tables 4 and 4-Suppl). In particular, doubling (or halving) the inlet flow-rate resulted in a difference of 68 % (27 %), 35 % (38 %), 52 % (112 %) in terms of mean TAWSS, OSI and RRT in the whole FPA model as compared to the reference model. As expected, the doubling (or halving) of the flow-rate was also associated with a reduction (or increase) of the lumen areas exposed low TAWSS, high OSI and RRT (see models  $M_{\text{walking}}$ ,  $M_{2Q}$  and  $M_{Q/2}$  in Figure 8 and Table 4). Finally, doubling (or halving) the period of walking resulted in a difference of 74 % (23 %), 68 % (9 %), 76 % (16 %) in terms of mean TAWSS, OSI and RRT in the whole vessel with respect to  $M_{\text{walking}}$ . The walking speed did not influence the location and extension of the lumen areas exposed to low TAWSS, which were almost absent in  $M_{\text{walking}}$ ,  $M_{T/2}$  and  $M_{2T}$ . Conversely, although the location was similar (Figure 8), the extension of the areas exposed to high OSI and RRT was different (Table 4).

#### 4. Discussion

At the present, the hemodynamics of patient-specific femoral arteries has been mainly analysed in straight leg configurations [11–18]. The main reason for this is that the geometrical models are reconstructed by means of techniques such as computed tomography or magnetic resonance imaging, for which the standard clinical protocol imposes the leg to be straight [16]. Solely in few recent works

[17,18], FPA hemodynamics was investigated by performing fixed-boundary CFD analyses in both straight and bent fixed configurations with the final aim to analyse the vessel kinking effect. It was noticed that the different knee-bending angle affected the WSS-based descriptors under consideration. Then, since the FPA displacement field is extremely wide, it could be even more important to understand which might be the impact of leg movement on hemodynamics. Therefore, the present work aimed at investigating whether the leg movements had minor or, instead, non-negligible influence on the velocity field and the shear stress along the luminal wall.

As expected, the instantaneous velocity field and cardiac cycle-averaged WSS-based descriptors, resulting from the fixed-boundary CFD analyses, changed substantially when comparing the bent leg configuration to the straight one. Furthermore, relevant differences were found between the moving-boundary models (i.e.  $M_{hip}$ ,  $M_{knee}$  and  $M_{walking}$ ) and the straight fixed leg configuration (i.e.  $F_0$ ), which is adopted in all the previous studies. In particular, from the quantitative comparisons between the moving- and fixed-boundary CFD analyses (Tables 1-3), it emerged that the leg movement was associated with higher values of mean TAWSS in the whole vessel model for all the three investigated movement types and smaller areas exposed to low TAWSS for the models  $M_{hip}$  and  $M_{walking}$ , as compared to  $F_0$ . Moreover, the leg movement introduced higher oscillatory shear stress, especially for  $M_{hip}$  and  $M_{walking}$ , which presented higher mean OSI in the whole vessel model and lumen areas exposed to high OSI than  $F_0$ . Considering the three portions of interest of the FPA (i.e. SFA, PA and TA), the impact of the leg movement on the WSS-based descriptors was different according to the movement type and the resultant effect of the inertial forces on blood flow. In particular, for the complete movement of walking, the highest differences were found in the SFA and TA portions, which are the most distant segments from the knee joint.

Differently from the coronary arteries, which are subjected to the cardiac-induced motion, the FPA undergoes the voluntary movement of the leg, which is completely independent from the heart beat. Hence, it was worth studying if a phase shift between the inlet flow-rate and the bending cycles could lead to a meaningful effect. The results showed that, among the characteristics studied in this

sensitivity analysis, the phase-shift was the least influential. On the contrary, the sensitivity analysis of the flow-rate and the walking speed revealed that both the parameters are extremely influential. Doubling (or halving) the flow-rate as well as doubling (or halving) the walking speed determined large modifications in the distributions of the WSS-based descriptors with high differences in the mean TAWSS, OSI and RRT in the whole vessel with respect to the reference model  $M_{\text{walking}}$  (Table 4).

Overall the FPA movement, although extremely simplified as in this study, was proved to widely alter the local hemodynamics and it could not be neglected in order to get the complete picture of the biomechanics of this vascular region. The results may suggest that the hip rotation and the complete walking are associated to negligible lumen areas exposed to low TAWSS, a condition that can be considered as atheroprotective. However, at the same time the lumen areas exposed to oscillatory shear stress (i.e. atheroprone regions) were larger as compared to the corresponding fixed-boundary models, highlighting that further studies should be conducted to better understand the complex interplay between local hemodynamics, leg movement type and atherosclerosis development in this vascular region. Similarly, the results of our sensitivity analysis in terms of OSI and RRT suggest that an increase in the walking speed (i.e. shorter bending period) may result in an atheroprone condition, with larger lumen areas exposed to high OSI and RRT. However, the lumen areas exposed to low TAWSS remained negligible, confirming the need of further investigation about the role of these hemodynamic descriptors in the onset and development of atherosclerosis in the FPA.

Although, to the best of the authors' knowledge, this is the first work in which the impact of leg movement on FPA hemodynamics was considered, several limitations are present. The geometrical model of FPA is idealized. All the geometrical features characterizing the patient-specific hemodynamics, including the minor side branches, were excluded from the analysis, and generic human-based dimensions regarding arterial length, diameter and deformation were used. Despite its simplification, this approach has the benefit to clearly point out the most influencing movement characteristics of the vessel, without the complexity of a patient-specific model. In a future

perspective, the numerical approach developed in the present work could be applied to patient-specific FPA models reconstructed from clinical images. Starting from an initial, straight vessel configuration, the aforementioned methodology could help investigate atheroprotective leg movements, with a view to a translational personalized therapy and rehabilitation. Another limitation is represented by the simulated leg movements, which are just a selection of all the possible dynamics of the lower limb. However, the presented method was proved to be effective in the more complex simulation of a gait cycle, featured by both knee and hip rotations. As regards the boundary conditions, the rigid wall condition was applied. However, a previous work on femoral arteries [29] demonstrated that the role of the arterial wall compliance is minimal on the local hemodynamics. In this study moving-boundary CFD analyses were performed. Nevertheless, to study the mechanical action of devices, such as self-expanding stents, or the effect of kinking of the arterial wall, the adoption of a fluid-structure interaction approach would be required, as previously done for coronary arteries [30]. In this case, a lumped parameter model could be also implemented and coupled to the 3D FPA model to consider the downstream vessel resistance. Finally, gravity was not included in the CFD models. Its effect on FPA local hemodynamics could be explored in a further study.

## 5. Conclusions

In the current study, an idealized CFD model of moving FPA was created. Moving-boundary CFD simulations replicating three different leg movements (i.e. hip rotation, knee flexion and walking) were compared to corresponding fixed-boundary analyses with straight or bent leg configuration. The results highlighted that the hemodynamics of femoral arteries is widely affected by leg movement, with non-negligible effects on both the instantaneous velocity field and the cardiac cycle-averaged WSS-based descriptors. Furthermore, the flow-rate curve amplitude and the bending period had a greater impact on the hemodynamics of the moving-boundary FPA model of walking as compared to the phase shift between cardiac and bending cycles.

The moving-boundary CFD analysis is a good approach to take into account the inertial effects introduced by leg movement. In a wider future perspective, the method here developed may be applied to patient-specific FPA models and allow the assessment of both device failure and luminal regions with a higher hemodynamic risk of atherosclerosis or restenosis.

**Conflict of interest:** None.

## Acknowledgments

M. Colombo, C. Chiastra and G. Pennati have been supported by Fondazione Cariplo, Italy (Grant number 2017-0792, TIME). The authors are very grateful to Manuela Galli who provided gait analysis data.

## References

- [1] Criqui MH, Aboyans V. Epidemiology of peripheral artery disease. *Circ Res* 2015;116:1509–26. doi:10.1161/CIRCRESAHA.116.303849.
- [2] Fowkes FGR, Aboyans V, Fowkes FJL, McDermott MM, Sampson UKA, Criqui MH. Peripheral artery disease: epidemiology and global perspectives. *Nat Rev Cardiol* 2016;14:156–70. doi:10.1038/nrcardio.2016.179.
- [3] Rymer JA, Jones WS. Femoropopliteal In-Stent Restenosis What Is the Standard of Care? *Circ Cardiovasc Interv* 2018;11:1–10. doi:DOI: 10.1161/CIRCINTERVENTIONS.118.007559.
- [4] Klein AJ, Chen SJ, Messenger JC, Hansgen AR, Plomondon ME, Carroll JD, et al. Quantitative assessment of the conformational change in the femoropopliteal artery with leg movement. *Catheter Cardiovasc Interv* 2009;74:787–98. doi:10.1002/ccd.22124.
- [5] Cheng CP, Wilson NM, Hallett RL, Herfkens RJ, Taylor CA. In vivo MR angiographic quantification of axial and twisting deformations of the superficial femoral artery resulting

from maximum hip and knee flexion. *J Vasc Interv Radiol* 2006;17:979–87.

doi:10.1097/01.RVI.0000220367.62137.e8.

- [6] MacTaggart JN, Phillips NY, Lomneth CS, Pipinos II, Bowen R, Timothy Baxter B, et al. Three-dimensional bending, torsion and axial compression of the femoropopliteal artery during limb flexion. *J Biomech* 2014;47:2249–56. doi:10.1016/J.JBIOMECH.2014.04.053.
- [7] Caro GG. Discovery of the role of wall shear in atherosclerosis. *Arterioscler Thromb Vasc Biol* 2009;29:158–61. doi:10.1161/ATVBAHA.108.166736.
- [8] Morbiducci U, Kok AM, Kwak BR, Stone PH, Steinman DA, Wentzel JJ. Atherosclerosis at arterial bifurcations: evidence for the role of haemodynamics and geometry. *Thromb Haemost* 2016;115:484–92. doi:10.1160/TH15-07-0597.
- [9] Chatzizisis YS, Coskun AU, Jonas M, Edelman ER, Feldman CL, Stone PH. Role of Endothelial Shear Stress in the Natural History of Coronary Atherosclerosis and Vascular Remodeling. *Molecular, Cellular, and Vascular Behavior. J Am Coll Cardiol* 2007;49:2379–93. doi:10.1016/j.jacc.2007.02.059.
- [10] Chiu J-J, Chien S. Effects of disturbed flow on vascular endothelium : pathophysiological basis and clinical perspectives. *Physiol Rev* 2011;91:327–87. doi:10.1152/physrev.00047.2009.
- [11] Li X, Liu X, Li X, Xu L, Chen X, Liang F. Tortuosity of the superficial femoral artery and its influence on blood flow patterns and risk of atherosclerosis. *Biomech Model Mechanobiol* 2019;18:883–96. doi:10.1007/s10237-019-01118-4.
- [12] Wood N, Zhao S, Zambanini A. Curvature and tortuosity of the superficial femoral artery: a possible risk factor for peripheral arterial disease. *J Appl Physiol* 2006;101:1412–8. doi:10.1152/jappphysiol.00051.2006.
- [13] Xu P, Liu X, Song Q, Chen G, Wang D, Zhang H, et al. Patient-specific structural effects on hemodynamics in the ischemic lower limb artery. *Sci Rep* 2016;6:39225. doi:10.1038/srep39225.

- [14] Gogineni A, Ravigururajan T. Flow dynamics and wall shear stresses in a bifurcated femoral artery. *J Biomed Eng Med Devices* 2017;2:1–9. doi:10.4172/2475-7586.1000130.
- [15] Javadzadegan A, Lotfi A, Simmons A, Barber T. Haemodynamic analysis of femoral artery bifurcation models under different physiological flow waveforms. *Comput Methods Biomech Biomed Engin* 2015;19:1143–53. doi:10.1080/10255842.2015.1113406.
- [16] Colombo M, Bologna M, Garbey M, Berceci S, He Y, Rodriguez Matas JF, et al. Computing patient-specific hemodynamics in stented femoral artery models obtained from computed tomography using a validated 3D reconstruction method. *Med Eng Phys* 2020;75:23–35. doi:10.1016/j.medengphy.2019.10.005.
- [17] Gökgöl C, Diehm N, Räber L, Büchler P. Prediction of restenosis based on hemodynamical markers in revascularized femoro-popliteal arteries during leg flexion. *Biomech Model Mechanobiol* 2019;18:1883–93. doi:10.1007/s10237-019-01183-9.
- [18] Desyatova A, Mactaggart J, Romarowski R, Poulson W, Conti M, Kamenskiy A. Effect of aging on mechanical stresses, deformations, and hemodynamics in human femoropopliteal artery due to limb flexion. *Biomech Model Mechanobiol* 2018;17:181–9. doi:10.1007/s10237-017-0953-z.
- [19] Wensing PJW, Scholten FG, Buijs PC, Hartkamp MJ, Mali WPTM, Hillen B. Arterial tortuosity in the femoropopliteal region during knee flexion : a magnetic resonance angiographic study 1995;187:133–9.
- [20] Wensing PJW, Meiss L, Mali WPTM, Hillen B. Early Atherosclerotic Lesions Spiraling Through the Femoral Artery. *Arterioscler Thromb Vasc Biol* 1998;18:1554–8. doi:10.1161/01.ATV.18.10.1554.
- [21] Lorbeer R, Grotz A, Dörr M, Völzke H, Lieb W, Kühn J-P, et al. Reference values of vessel diameters, stenosis prevalence, and arterial variations of the lower limb arteries in a male population sample using contrast-enhanced MR angiography. *PLoS One* 2018;13:e0197559. doi:10.1371/journal.pone.0197559.

- [22] Wolf YG, Kobzantsev Z, Zelmanovich L. Size of normal and aneurysmal popliteal arteries: A duplex ultrasound study. *J Vasc Surg* 2006;43:488–92. doi:10.1016/j.jvs.2005.11.026.
- [23] Klein WM, Bartels LW, Bax L, Van Der Graaf Y. Magnetic resonance imaging measurement of blood volume flow in peripheral arteries in healthy subjects. *J Vasc Surg* 2003;38:1060–6. doi:10.1016/S0741-5214(03)00706-7.
- [24] Luraghi G, Wu W, De Castilla H, Rodriguez Matas JF, Dubini G, Dubuis P, et al. Numerical Approach to Study the Behavior of an Artificial Ventricle: Fluid–Structure Interaction Followed By Fluid Dynamics With Moving Boundaries. *Artif Organs* 2018;42:E315–24. doi:10.1111/aor.13316.
- [25] Gökgöl C, Diehm N, Nezami FR, Büchler P. Nitinol stent oversizing in patients undergoing popliteal artery revascularization: a finite element study. *Ann Biomed Eng* 2015;43:2868–80. doi:10.1007/s10439-015-1358-8.
- [26] Poulson W, Kamenskiy A, Seas A, Deegan P, Lomneth C, MacTaggart J. Limb flexion-induced axial compression and bending in human femoropopliteal artery segments. *J Vasc Surg* 2018;67:607–13. doi:10.1016/j.jvs.2017.01.071.
- [27] De Nisco G, Kok AM, Chiastra C, Gallo D, Hoogendoorn A, Migliavacca F, et al. The Atheroprotective Nature of Helical Flow in Coronary Arteries. *Ann Biomed Eng* 2019;47:425–38. doi:10.1007/s10439-018-02169-x.
- [28] Gallo D, Steinman DA, Morbiducci U. Insights into the co-localization of magnitude-based versus direction-based indicators of disturbed shear at the carotid bifurcation. *J Biomech* 2016;49:2413–9. doi:10.1016/j.jbiomech.2016.02.010.
- [29] Kim Y-H, Kim J-E, Ito Y, Shih AM, Brott B, Anayiotos A. Hemodynamic Analysis of a Compliant Femoral Artery Bifurcation Model using a Fluid Structure Interaction Framework. *Ann Biomed Eng* 2008;36:1753–63. doi:10.1007/s10439-008-9558-0.
- [30] Bukač M, Čanić S, Tambača J, Wang Y. Fluid–structure interaction between pulsatile blood flow and a curved stented coronary artery on a beating heart: A four stent computational

study. Comput Methods Appl Mech Eng 2019;350:679–700. doi:10.1016/j.cma.2019.03.034.

Post-Print

## Tables

**Table 1.** Comparison between the moving-boundary model  $M_{hip}$  and the corresponding fixed-boundary models  $F_0$ , in terms of mean values of time-averaged wall shear stress (TAWSS), oscillatory shear index (OSI) and relative residence time (RRT) along the entire lumen (Total) and the region-specific luminal surfaces (i.e., superficial femoral artery (SFA), popliteal artery (PA) and tibial artery (TA)), and of percentage lumen areas exposed to TAWSS30, OSI66 and RRT66.

		$M_{hip}$	$F_0$
<b>TAWSS [Pa]</b>	Total	1.85	0.63
	SFA	1.95	0.66
	PA	1.80	0.63
	TA	1.84	0.62
<b>OSI [-]</b>	Total	0.35	0.16
	SFA	0.35	0.14
	PA	0.35	0.16
	TA	0.35	0.16
<b>RRT [Pa<sup>-1</sup>]</b>	Total	2.10	2.44
	SFA	2.27	2.63
	PA	2.00	2.35
	TA	2.12	2.41
<b>%TAWSS33</b>	Total	0%	24%
<b>%OSI66</b>	Total	99%	0%
<b>%RRT66</b>	Total	29%	1%

**Table 2.** Comparison between the moving-boundary model  $M_{knee}$  and the corresponding fixed-boundary models  $F_0$ ,  $F_{45}$  and  $F_{90}$ , in terms of mean values of time-averaged wall shear stress (TAWSS), oscillatory shear index (OSI) and relative residence time (RRT) along the entire lumen (Total) and the region-specific luminal surfaces (i.e., superficial femoral artery (SFA), popliteal artery (PA) and tibial artery (TA)), and of percentage lumen areas exposed to TAWSS30, OSI66 and RRT66.

		$M_{knee}$	$F_0$	$F_{45}$	$F_{90}$
<b>TAWSS [Pa]</b>	Total	0.73	0.63	0.64	0.65
	SFA	0.64	0.66	0.66	0.68
	PA	0.69	0.63	0.64	0.63
	TA	0.88	0.62	0.62	0.66
<b>OSI [-]</b>	Total	0.14	0.16	0.14	0.13
	SFA	0.13	0.14	0.14	0.12
	PA	0.13	0.16	0.14	0.15
	TA	0.17	0.16	0.15	0.12
<b>RRT [Pa<sup>-1</sup>]</b>	Total	2.16	2.44	2.36	2.29
	SFA	2.63	2.63	2.61	2.85
	PA	2.05	2.35	2.23	2.30
	TA	1.88	2.41	2.38	2.15
<b>%TAWSS33</b>	Total	36%	24%	40%	48%
<b>%OSI66</b>	Total	1%	0%	0%	1%
<b>%RRT66</b>	Total	10%	1%	13%	12%

**Table 3.** Comparison between the moving-boundary model  $M_{\text{walking}}$  and the corresponding fixed-boundary models  $F_0$ ,  $F_{13}$  and  $F_{58}$ , in terms of mean values of time-averaged wall shear stress (TAWSS), oscillatory shear index (OSI) and relative residence time (RRT) along the entire lumen (Total) and the region-specific luminal surfaces (i.e., superficial femoral artery (SFA), popliteal artery (PA) and tibial artery (TA)), and of percentage lumen areas exposed to TAWSS30, OSI66 and RRT66.

		$M_{\text{walking}}$	$F_0$	$F_{13}$	$F_{58}$
<b>TAWSS [Pa]</b>	Total	0.88	0.63	0.60	0.61
	SFA	0.93	0.66	0.64	0.57
	PA	0.84	0.63	0.60	0.61
	TA	0.93	0.62	0.59	0.62
<b>OSI [-]</b>	Total	0.24	0.16	0.15	0.13
	SFA	0.25	0.14	0.12	0.15
	PA	0.23	0.16	0.15	0.13
	TA	0.24	0.16	0.15	0.12
<b>RRT [Pa<sup>-1</sup>]</b>	Total	2.38	2.44	2.69	2.60
	SFA	2.47	2.63	3.38	2.66
	PA	2.35	2.35	2.42	2.31
	TA	2.37	2.41	2.45	2.70
<b>%TAWSS33</b>	Total	1%	24%	94%	74%
<b>%OSI66</b>	Total	54%	0%	0%	0%
<b>%RRT66</b>	Total	36%	1%	13%	15%

**Table 4.** Quantitative results of the sensitivity analysis in terms of wall shear stress (WSS) based descriptors (reference  $M_{\text{walking}}$ ): mean values of the descriptors along the entire lumen (Total) and the region-specific luminal surfaces (i.e., superficial femoral artery (SFA), popliteal artery (PA) and tibial artery (TA)), and percentage lumen areas exposed to TAWSS30, OSI66 and RRT66.

		$M_{\text{walking}}$	$M_{\text{phase}}$	$M_{2Q}$	$M_{Q2}$	$M_{T12}$	$M_{2T}$
<b>TAWSS [Pa]</b>	Total	0.88	0.69	1.47	0.65	1.53	0.68
	SFA	0.93	0.64	1.55	0.67	1.61	0.72
	PA	0.84	0.64	1.41	0.60	1.39	0.66
	TA	0.93	0.84	1.52	0.72	1.72	0.67
<b>OSI [-]</b>	Total	0.24	0.21	0.16	0.33	0.40	0.22
	SFA	0.25	0.19	0.17	0.35	0.41	0.22
	PA	0.23	0.21	0.15	0.33	0.41	0.22
	TA	0.24	0.23	0.16	0.33	0.39	0.21
<b>RRT [Pa<sup>-1</sup>]</b>	Total	2.38	2.77	1.13	5.04	4.18	2.77
	SFA	2.47	2.74	1.21	5.60	4.97	2.78
	PA	2.35	3.13	1.07	5.00	4.32	2.74
	TA	2.37	2.50	1.14	4.57	3.16	2.81
<b>%TAWSS33</b>	Total	1%	44%	1%	63%	0%	1%
<b>%OSI66</b>	Total	54%	27%	18%	97%	98%	44%
<b>%RRT66</b>	Total	36%	62%	1%	96%	88%	62%

## Figure captions

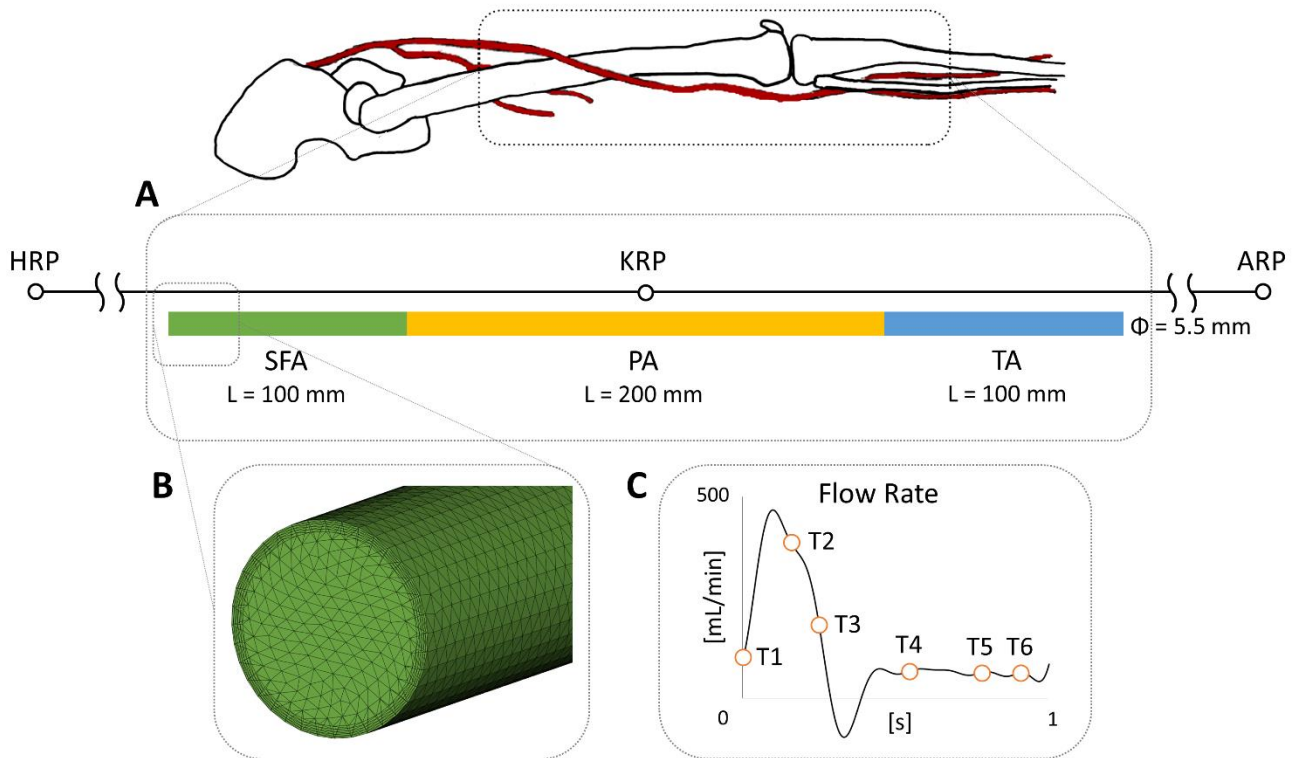


**Figure 1.** Idealized model of the femoropopliteal artery. **A)** Geometrical model of the portion of interest, built as a regular cylinder with a diameter of 5.5 mm and a length of 400 mm. The proximal part (green) corresponds to the superficial femoral artery (SFA); the middle part (yellow) to the popliteal artery (PA); the distal part (blue) to the first portion of the tibial artery (TA). Articular joints of the hip (HRP), the knee (KRP), and the ankle (ARP) are also shown. **B)** Detail of the computational grid of the model with tetrahedral elements and prismatic boundary layers at the wall. **C)** Triphasic flow-rate curve [16], typical of the femoral region, applied as inflow boundary condition.

T1=0s, T2=0.1 s, T3=0.25s, T4=0.5s, T5=0.75 s, T6=0.9 s.

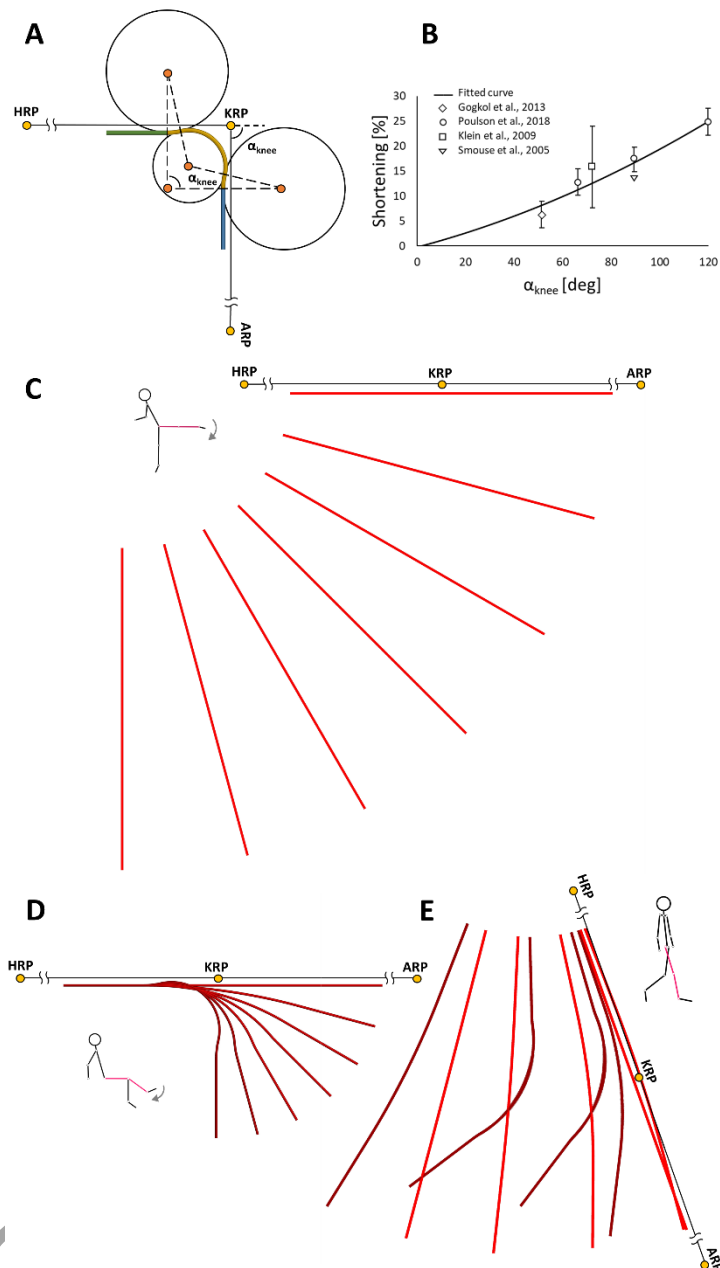


**Figure 2.** Configurations of the movements of the FPA model. **A)** Example of vessel geometry construction using three circumference arcs to draw the bent popliteal artery segment for  $\alpha_{knee}$  of  $90^\circ$ . **B)** Percentage of shortening with respect to the increasing of the flexion angle  $\alpha_{knee}$ : curve derived from the fitting of four literature data. **C)** Centerlines of seven configurations used to guide the wall displacement of model  $M_{hip}$ . **D)** Centerlines of seven configurations used to guide the wall displacement of model  $M_{knee}$ . **E)** Representation of the nine configurations' centerlines used to guide the wall displacement of model  $M_{walking}$ , obtained from gait analysis data.

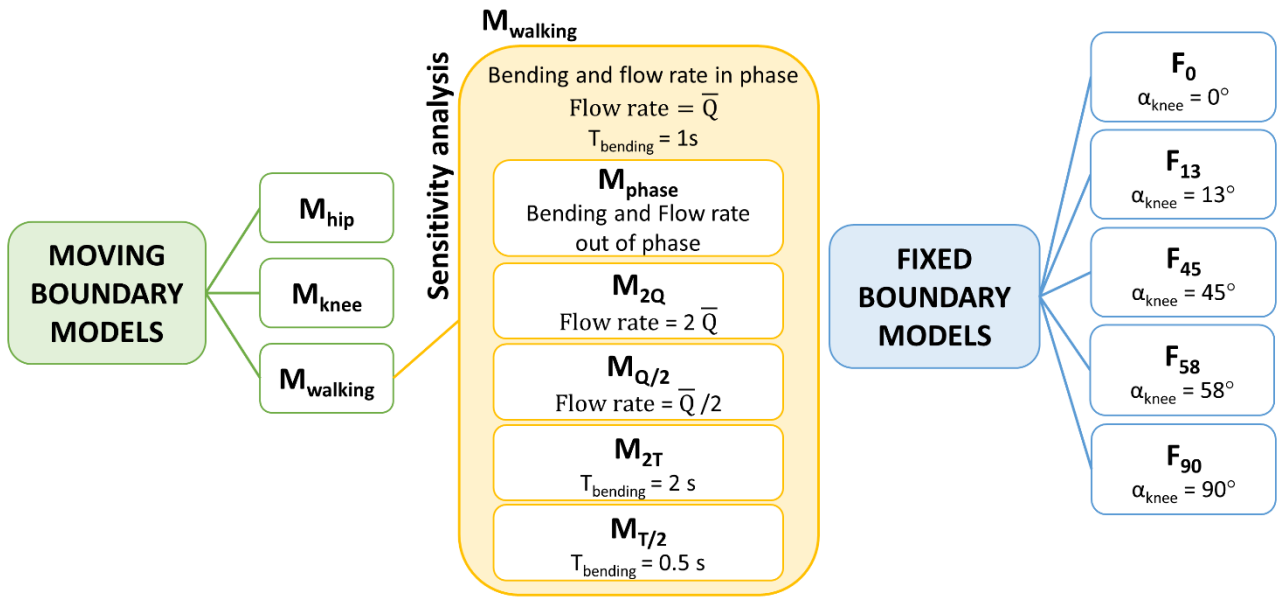


**Figure 3.** Sketch of all test scenarios defined to perform the simulations.

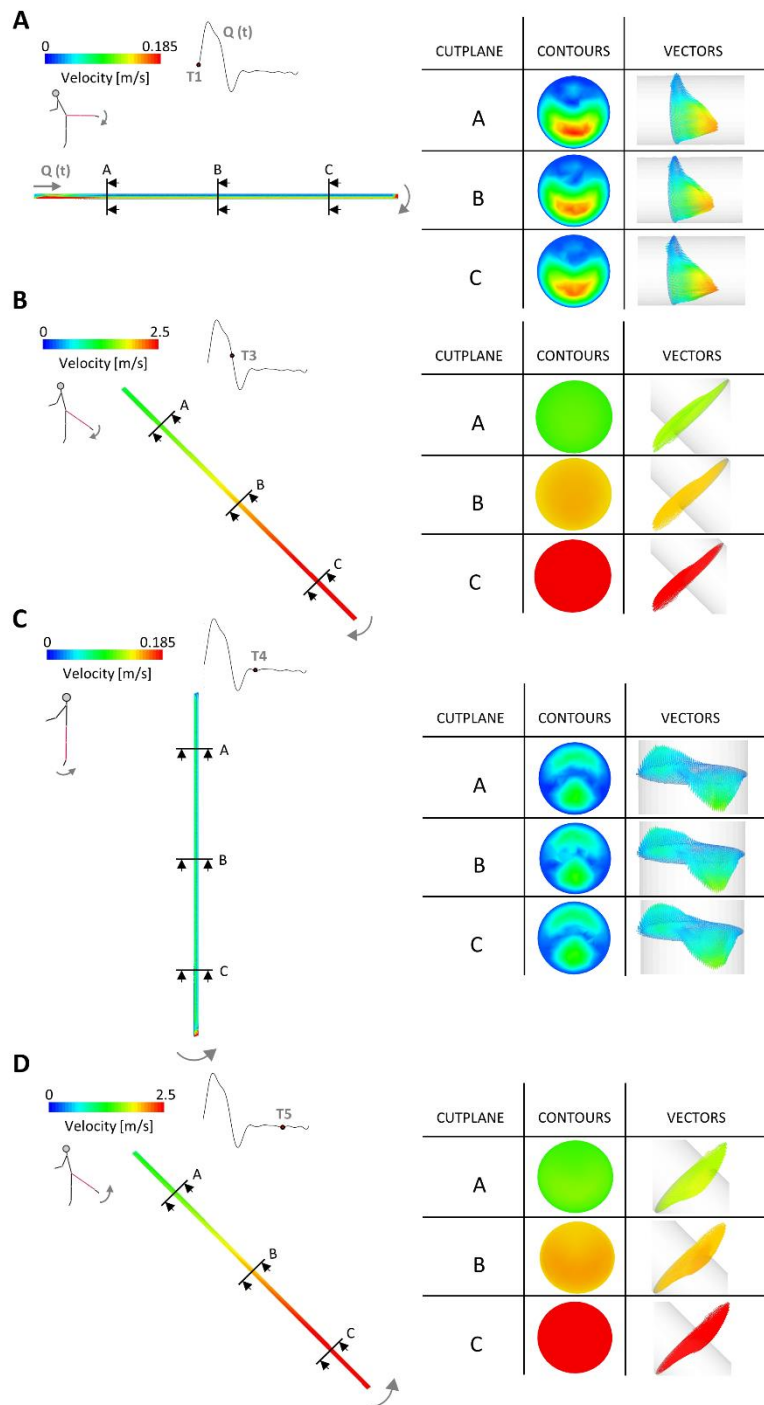


**Figure 4.** Velocity field of model  $M_{hip}$  at four different instants during the cardiac cycle with  $\alpha_{hip}$  of  $0^\circ$  (A – T1),  $45^\circ$  (B – T3 and D – T5) and  $90^\circ$  (C – T4). On the left, the contour maps of velocity magnitude are shown on the longitudinal section. On the right, the contour maps of velocity magnitude as well as the velocity vectors are depicted for three transversal sections of interest.

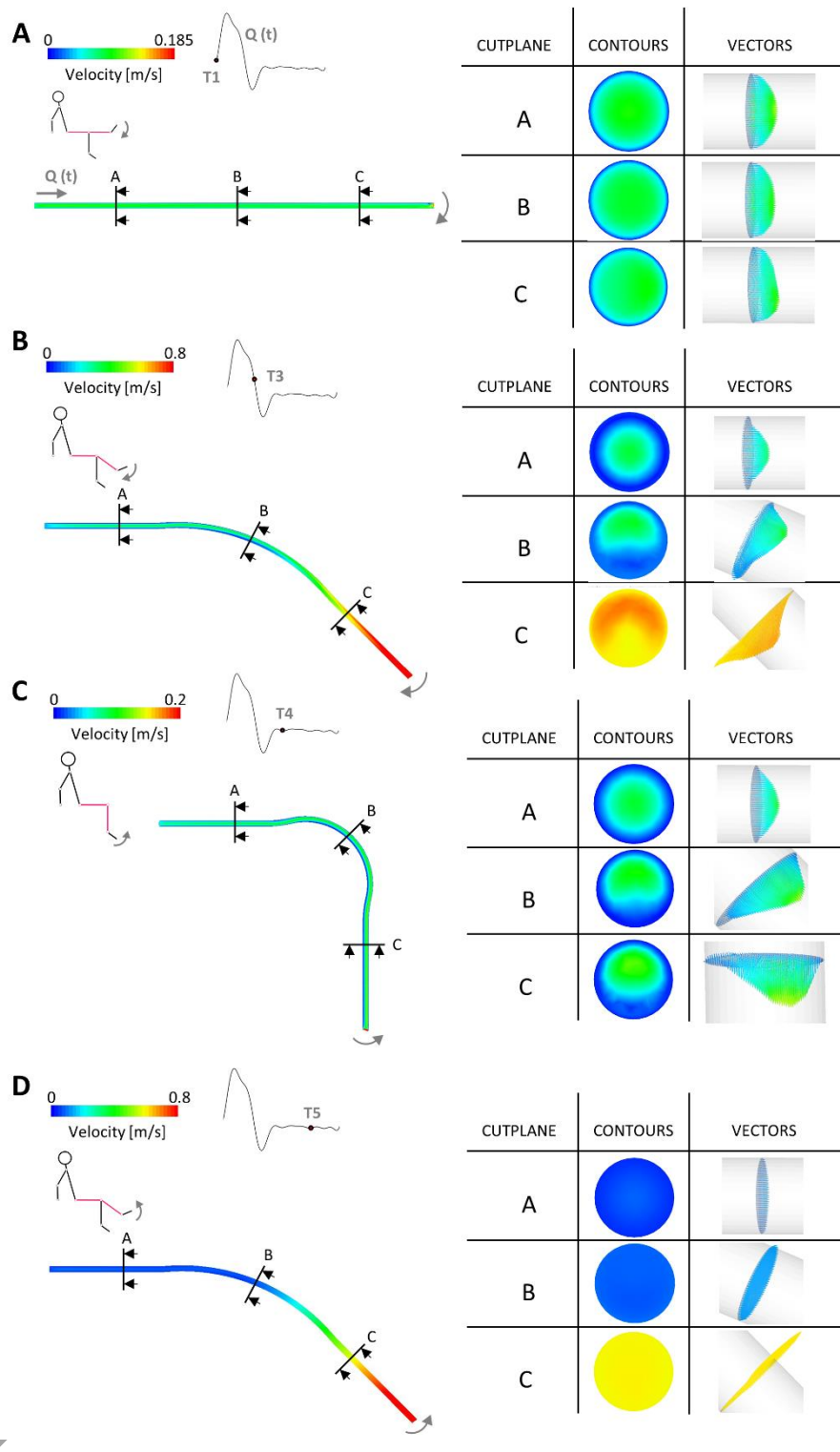


**Figure 5.** Velocity field of model  $M_{knee}$  at four different instants during the cardiac cycle with  $\alpha_{knee}$  of  $0^\circ$  (A – T1),  $45^\circ$  (B – T3 and D – T5) and  $90^\circ$  (C – T4). On the left, the contour maps of velocity magnitude are shown on the longitudinal section. On the right, the contour maps of velocity magnitude as well as the velocity vectors are depicted for three transversal sections of interest.

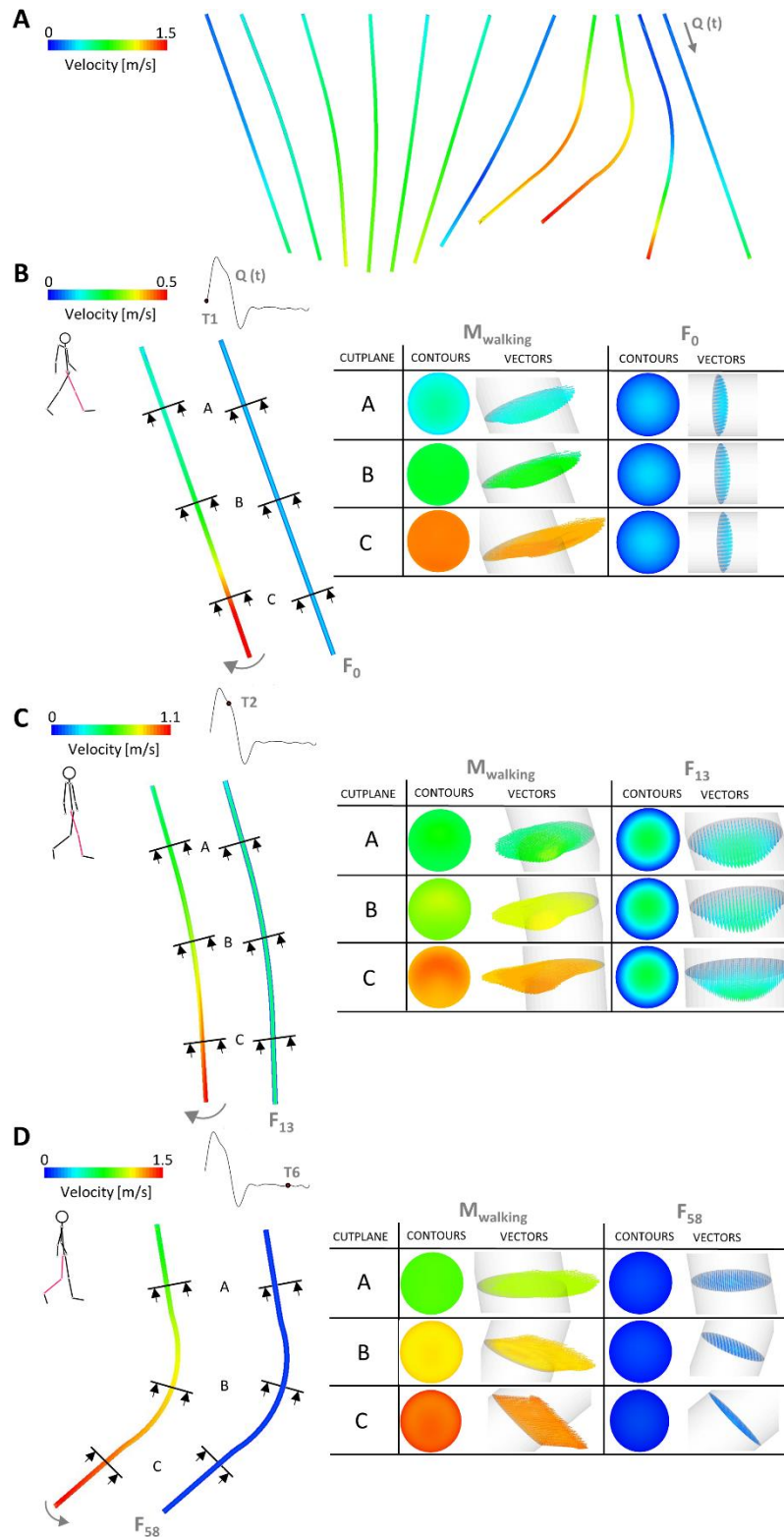


**Figure 6.** Velocity field of model  $M_{walking}$  during one walking cycle (A) and at three different instants during the cardiac cycle with  $\alpha_{knee}$  of  $0^\circ$  (B – T1),  $13^\circ$  (C – T2) and  $58^\circ$  (D – T6). The contour maps of the velocity magnitude on the longitudinal section and on three different transversal sections of interest, including the velocity vectors, are shown.

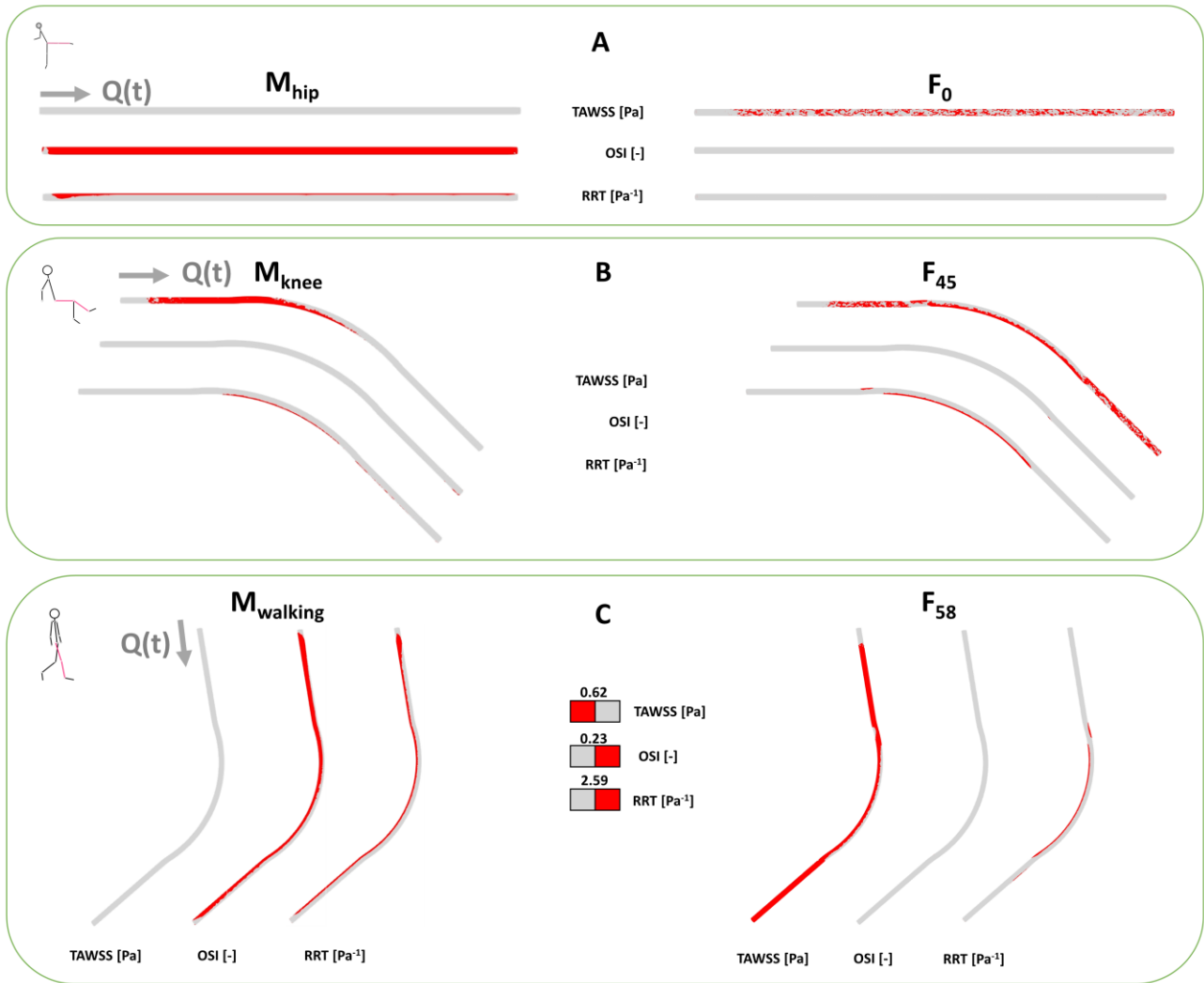


**Figure 7.** Comparison of lumen areas exposed to TAWSS33, OSI66 and RRT66 between the models  $M_{\text{walking}}$  and  $F_{58}$  (A),  $M_{\text{knee}}$  and  $F_{45}$  (B), and  $M_{\text{hip}}$  and  $F_0$  (C).

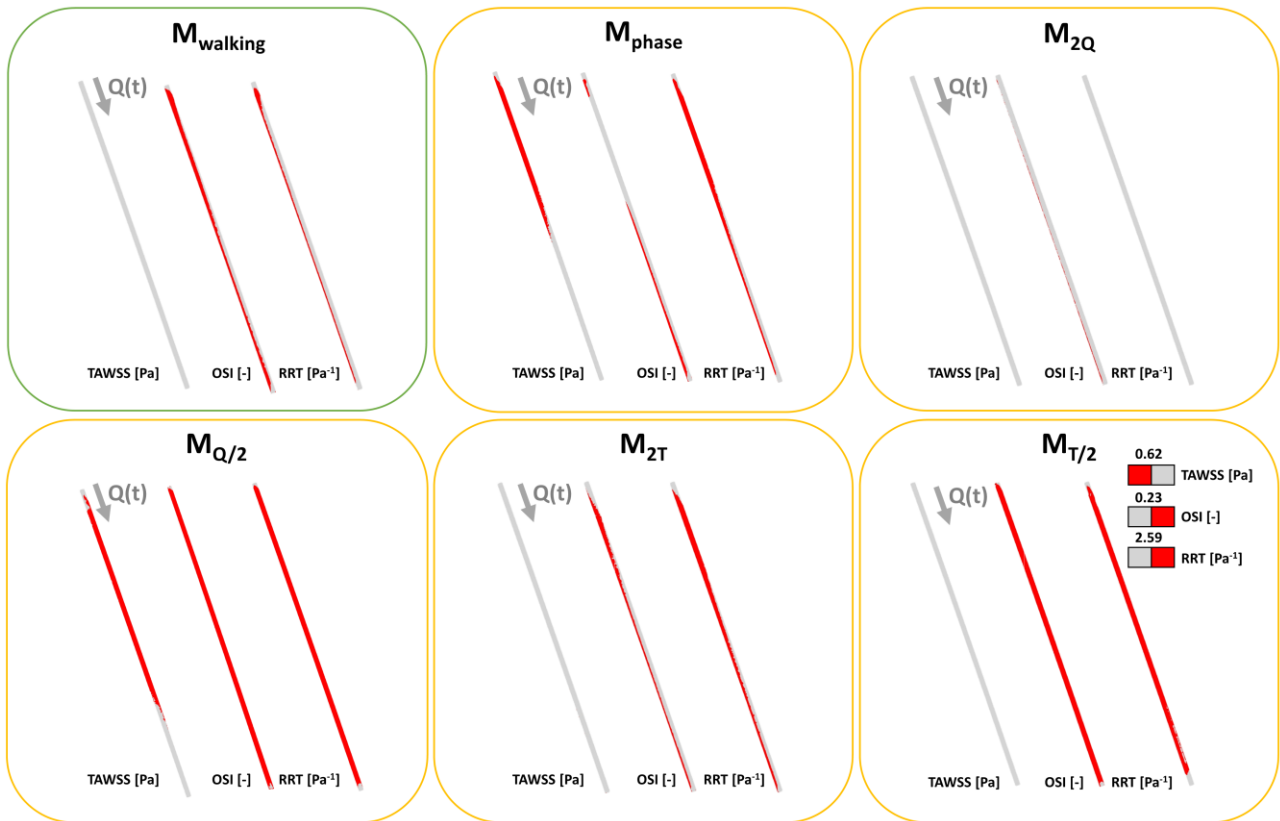


**Figure 8.** Comparison of lumen areas exposed to TAWSS33, OSI66 and RRT66 among the reference moving model  $M_{\text{walking}}$ , the counter-phase model  $M_{\text{phase}}$ , the doubled flow-rate model  $M_{2Q}$ , the halved flow-rate model  $M_{Q/2}$ , the slow-moving model  $M_{2T}$  and the fast-moving model  $M_{T/2}$ . The hemodynamic descriptors are plotted in the straight vessel configuration.